KeAi

CHINESE ROOTS
GLOBAL IMPACT

Contents lists available at ScienceDirect

Petroleum Science

journal homepage: www.keaipublishing.com/en/journals/petroleum-science



Original Paper

Risk assessment of fault reactivation considering the heterogeneity of friction strength in the BZ34-2 Oilfield, Huanghekou Sag, Bohai Bay Basin, China



Ye-Jun Jin ^{a, b}, Ling-Dong Meng ^{b, c, *}, Ding-You Lyu ^d, Xiao-Fei Fu ^{a, b}, Jiang-Bo Huang ^d, Si-Jia Cao ^a, Jian-Da Li ^a

- ^a School of Earth Sciences, Northeast Petroleum University, Daqing 163318, Heilongjiang, China
- b Key Laboratory of Oil & Gas Reservoir and Underground Gas Storage Integrity Evaluation of Heilongjiang Province, Northeast Petroleum University, Daqing 163318, Heilongjiang, China
- ^c Bohai Rim Energy Research Institute, Northeast Petroleum University, Qinhuangdao, 066004, Hebei, China
- ^d CNOOC Tianjin Company, Tianjin 300459, China

ARTICLE INFO

Article history: Received 7 April 2022 Received in revised form 1 January 2023 Accepted 20 June 2023 Available online 21 June 2023

Edited by Jie Hao and Teng Zhu

Keywords:
Fault reactivation
In-situ stress
Strength heterogeneity of fault friction
Huanghekou Sag

ABSTRACT

The hazards of fault reactivation caused by fluid injection are a growing concern, However, traditional evaluation methods of fault stability are likely to underestimate the risk in fault segments with a high clay content. Therefore, an extended evaluation method of fault stability (ECPP) incorporating the heterogeneity in friction strength caused by variation in the clay content within the fault zone is established in this study. After characterizing the current stress field of the BZ34-2 Oilfield in the Huanghekou Sag, Bohai Bay Basin, the reactivation potential of faults is evaluated using both traditional and ECPP methods. Traditional evaluation of fault stability shows that all faults are stable in the present stress field. Faults oriented ENE have a relatively high risk. The maximum sustainable fluid pressure Δp is approximately 8.8 -8.9 MPa and 9.3-9.9 MPa. When considering the heterogeneity in fault friction strength, the fault stability is clearly controlled by the clay content of the faults. The high-risk fault segments assessed using traditional methods are no longer obvious, which reflects the importance of incorporating friction strength heterogeneity in the process of fault evaluation. Moreover, the results also show that most fault segments are activated when the fault zone is dominated by montmorillonite, reflecting the strong influence of clay mineral types on fault stability. The factors influencing the heterogeneity of fault friction strength are very complicated in actual situations. Therefore, future work should focus on establishing a database through a large number of experiments and investigating the relationship between the friction coefficient and the main controlling factors.

© 2023 The Authors. Publishing services by Elsevier B.V. on behalf of KeAi Communications Co. Ltd. This is an open access article under the CC BY-NC-ND license (http://creativecommons.org/licenses/by-nc-nd/4.0/).

1. Introduction

The risk of fault reactivation is important in many fields related to geological engineering, e.g., fluid waste disposal (Ellsworth, 2013; Manga et al., 2016; McGarr and Barbour, 2017), storage of CO₂ (Kaven et al., 2015; Gamboa et al., 2019; Williams-Stroud et al., 2020), storage of natural gas (Cesca et al., 2014; Meng et al., 2017; Zhang et al., 2022), and enhanced oil recovery (EOR) (Gan and

E-mail address: Lingdong.Meng@hotmail.com (L.-D. Meng).

Frohlich, 2013; Amiri et al., 2019). Injecting a massive volume of fluid into a fault-bounded reservoir increases the reservoir pressure, reduces the effective normal stress acting on preexisting faults, and eventually results in fault reactivation, as indicated by Amonton's law (Jaeger and Cook, 1979).

Earthquakes are a form of fault reactivation, many of which are induced by massive fluid injection (Healy et al., 1968; Raleigh et al., 1976; Zoback and Harjes, 1997; Ellsworth, 2013; McGarr and Barbour, 2017), and quite a few have magnitudes greater than 6 according to the HiQuake database (Wilson et al., 2017). The potential hazards of such reactivation have been investigated by many researchers in the past decade, e.g., casing shear failure (Dusseault

^{*} Corresponding author. Bohai Rim Energy Research Institute, Northeast Petroleum University, Qinhuangdao, 066004, China.

Y.-J. Jin, L.-D. Meng, D.-Y. Lyu et al. Petroleum Science 20 (2023) 2695–2708

et al., 2001; Mohammed et al., 2019; Xi et al., 2019), breaching trap integrity by creating or enhancing leakage conduits (Wiprut and Zoback, 2002; Langhi et al., 2010), fluid escape to the seafloor by seafloor-connected faults (Liu and Xi, 2012), and borehole instability during drilling (Willson et al., 1999).

Given this, many evaluation methods have been established to recognize potential risky fault segments, such as Ts—slip tendency (Morris et al., 1996), Td—dilation tendency (Ferrill et al., 1999), CFF—Coulomb failure function (Castillo et al., 2000), CPP—critical pressure perturbation (Wiprut and Zoback, 2002) and FAST-fault analysis seal technology (Mildren et al., 2005). The difference between CPP and FAST is that the latter incorporates the cohesive strength of faults, which is often negligible for shallow faults, and the other details of these methods have been summarized in (Mildren et al., 2005). However, in the process of fault stability evaluation using the above parameters, the friction coefficient of the whole fault is often set to 0.6 or another single value (Wiprut and Zoback, 2002; Mildren et al., 2005; Schwab et al., 2017; Leclère and Calais, 2019), and there is no consideration of the heterogeneity in fault friction strength, which is controlled by many factors, e.g., clay content (it refers to volume percentage in this paper) (Shimamoto and Logan, 1981; Takahashi et al., 2007; Tembe et al., 2010), particle characteristics (Anthony and Marone, 2005), wetness (Morrow et al., 2000; Bullock et al., 2015), temperature (Verberne et al., 2010; Zhang and He, 2013), and effective normal stress (Saffer and Marone, 2003; Moore and Lockner, 2008; Behnsen and Faulkner, 2012; Haines et al., 2013). The effect of clay content on friction strength is particularly significant, and the difference in the friction coefficient between pure sandstone and clay is mostly located at 0.41–0.58 according to the statistics from Meng et al. (2017). However, for a fault developed in a reservoir with a small depth range, other factors will not change significantly except for the fault clay content. In addition, compared with other factors, the influence of fault clay content on friction strength is more obvious (Shimamoto and Logan, 1981; Logan and Rauenzahn, 1987; Brown et al., 2003; Saffer and Marone, 2003; Takahashi et al., 2007; Crawford et al., 2008; Tembe et al., 2010). Given this, Meng et al. (2017) attempted to integrate the heterogeneity of friction strength into the evaluation of fault stability. However, the method used in the paper is to take three fixed values in the clay content ranges of 0%-20%, 20%-40% and 40%-100%, which is not very suitable for actual geological situations due to the lack of continuity of the fault friction coefficient. At the same time, the influence of clay mineral types on fault stability has not been analyzed.

BZ34-2 is an offshore oilfield that began depleted production in June 1990 (Zhou et al., 2005). After a very short time, the oilfield entered the water injection stage in September 1992. During the 30 years of water injection, scholars have not paid much attention to the in-situ stress and fault risk, and no relevant literature has been published. In view of the hazards of fault reactivation to oilfield production, ecosystems and human habitations, it is critical to analyze the geological characteristics of risky fault segments and determine the maximum sustainable fluid pressure (Δp) for safe and efficient production.

Therefore, following Meng et al. (2017), the extended evaluation method for fault stability is established considering the heterogeneity of fault friction strength caused by the variation in clay content within fault zones in this paper. To illustrate the necessity of this extended method, the faults of the BZ34-2 Oilfield are evaluated under two cases with Δp (see below for more detail) as the comparison parameter, based on the in-situ stress interpretation results. In one case, the friction coefficient is set to 0.6, and in other cases, the friction coefficient is set as a function of the fault clay content.

2. Geological setting

The Bohai Bay Basin is the most petroliferous basin in China, accounting for nearly one-third of the total oil production of the country (Hao et al., 2010; Tian et al., 2014; Wang et al., 2022). Many scholars believe that the Bohai Bay Basin is a Cenozoic rift basin reformed by syngenetic strike-slip faults, including the western Taihangshan fault and eastern Tan-Lu fault (Hsiao et al., 2004: Oi and Yang, 2010). It underwent a synrifting stage in the Paleogene and a postrifting thermal subsidence stage from the Neogene to the present (Allen et al., 1997; Hsiao et al., 2004; Mao et al., 2019, 2021). The regional stress orientation of the Bohai Bay Basin is NEE (Hu et al., 2017), mainly from the combined effect of Pacific plate subduction and the push of the Philippine plate (Hu et al., 2017). Located in the eastern Bohai Bay Basin (Fig. 1a), the Huanghekou Sag is in a half-graben shape, which faults in the northern part and overlaps in the southern part, with the Bonan uplift to the north and the Laibei uplift to the south (Sun et al., 2011).

The BZ34-2 Oilfield is located in the center of the Huanghekou Sag, Bohai Bay Basin (Fig. 1a) and is characterized by a faulted anticline with two sets of NE-striking and nearly E-W-striking normal faults (Fig. 1b). The Shahejie Formation, composed of lower Oligocene and upper Eocene strata, is one of the main oil-bearing intervals with fan delta deposits. The reservoir is dominated by feldspar-quartz sandstone, with grains that are poorly rounded and sorted and with a porosity range of 8.6–16.9% and a permeability range of $0.5-330 \times 10^{-3} \, \mu m^2$ (Wang, 2016). The oilfield is divided into the North Block (bounded by faults F15, F30, F31 and F32), the Central Block (bounded by faults F30 and F31) and the South Block (bounded by faults F31, F35, and F68) (Fig. 1b). The North Block and the Central Block, the target areas of this study, are the main oil production regions and feature a relatively high well density. The Shahejie Formation can be divided into four oil-bearing members: Mbr 1 (developed only in the South Block), Mbr 2, Mbr 3 and Mbr 4 from top to bottom with burial depths of 3000-3500 m. The three blocks have different OWCs (Fig. 1c), indicating that the partial trap-boundary faults (F30, F31, F32 and F15) are sealing, which will result in overpressurization during water injection and may cause the fault to slip. Note that the Penglai19-3 Oilfield, located approximately 54 km to the northeast of the BZ34-2 Oilfield (Fig. 1a), is an example of oil seepage to the seafloor due to a high injection pressure (Liu and Xi, 2012). Therefore, the injection pressure should be minimized to prevent fault slippage, but this is not conducive to an increase in oil field productivity. Therefore, the critical pore pressure of the faults needs to be predicted to optimize the injection pressure.

3. Data and methods

3.1. Traditional evaluation method of fault reactivation

According to brittle failure theory (Jaeger and Cook, 1979), the stability of faults is mainly controlled by the stress acting on the fault plane, pore pressure, fault friction coefficient, and fault cohesion. For an ideal flat fault plane, the normal stress and shear stress can be calculated by Eqs. (1) and (2), corresponding to one point in the normal stress and shear stress coordinate system (Fig. 2). However, the actual fault surface is always irregular. In this case, the fault surface needs to be divided into small elements to calculate their stress state and then analyze the reactivation possibility of every fault element (Streit, 1999; Gamboa et al., 2019). An increase in the pore fluid pressure will result in all effective principal stresses decreasing by the same magnitude, which eventually causes Mohr's circle to move to the left. As the pore pressure

Y.-J. Jin, L.-D. Meng, D.-Y. Lyu et al. Petroleum Science 20 (2023) 2695–2708

increases by Δp , the point representing a fault element will touch the envelope, indicating that the corresponding fault element will begin to slip or dilate (Wiprut and Zoback, 2002; Taghipour et al., 2019). Hence, it is a good way to use Δp , the fluid pressure required for fault slip from its initial state to the critical stress state, to describe the likelihood of fault reactivation. $\Delta p > 0$ indicates that additional fluid pressure can still be sustained; conversely, $\Delta p \leq 0$ indicates that a fault element is in a critical stress state and has great potential for reactivation.

$$\sigma_{n} = \sigma_{1} \cos^{2} \alpha_{n} + \sigma_{2} \cos^{2} \beta_{n} + \sigma_{3} \cos^{2} \gamma_{n}$$
 (1)

$$\tau = \sqrt{\sigma_1^2 \cos^2 \alpha_n + \sigma_2^2 \cos^2 \beta_n + \sigma_3^2 \cos^2 \gamma_n - \sigma_n^2}$$
 (2)

where σ_n and τ are the effective normal stress and shear stress, respectively; σ_1 , σ_2 and σ_3 are the maximum, intermediate and minimum effective principal stresses, respectively; and α_n , β_n , and γ_n are the angles between the effective principal stresses and the normal to the fault element (Fig. 2).

The cohesion of a preexisting fault is generally heterogeneous in the range from 0 to 10 MPa (Meng et al., 2017), which is often neglected for shallow faults; therefore, Δp can be expressed as follows ($\Delta p_{\text{incohesive}}$ in Fig. 3):

$$\Delta p = \sigma_{\rm n} - \tau/\mu \tag{3}$$

According to Wiprut and Zoback (2002), Eq. (3) is the form of critical pressure perturbation (CPP). In a traditional evaluation process, the coefficient of static friction μ is recommended to be set to 0.6 (Zoback, 2007; Sibson, 2017).

3.2. Extended evaluation method of fault reactivation

However, the friction strength of different parts of the fault will show some heterogeneity due to the influence of the fault gouge, and the overall trend was a decrease in strength with increasing clay content (Shimamoto and Logan, 1981; Takahashi et al., 2007; Tembe et al., 2010). The weakening effect of the fault gouge on the friction strength is mainly controlled by three mechanisms. The first is the particle characteristics, such as size, shape and roughness (Anthony and Marone, 2005). In friction deformation, fault rock with a large particle size and high grain angularity requires additional shear stress to generate a larger expansion space for rolling deformation, so fine-grained and ultrafine-grained fault gouges have relatively low friction strength. Second, most clay minerals have a layered structure (Summers and Byerlee, 1977), and bonding forces between structural layers are lower than those in nonlayered-structure minerals, resulting in a lower friction strength for clay minerals. Third, foliated structures are usually developed in clay minerals (Collettini et al., 2009; Hellebrekers et al., 2019); these structures are smooth planar structures that can restrain cataclasis and have less frictional resistance than other parts of fault zones, which significantly weakens the macroscopic frictional strength of a fault.

Based on the CPP, this paper establishes the extended method for fault stability evaluation (ECPP) incorporating the heterogeneity in friction strength caused by variation in the clay content within fault zones. Therefore, Δp can be expressed by the following equation:

$$\Delta p = \sigma_{\rm n} - \tau / \mu(V_{\rm sh}) \tag{4}$$

where $V_{\rm sh}$ is the fault clay content and $\mu(V_{\rm sh})$ is the friction coefficient as a function of $V_{\rm sh}$. For the calculation of fault clay content, the most widely used is the shale gouge ratio (SGR) algorithm

(Knipe et al., 1997; Yielding et al., 1997; Pei et al., 2015), which is also often used as a proxy for fault zone heterogeneity to evaluate the heterogeneous permeability of faults and to predict the hydrocarbon column height sealed by faults (Eq. (5)).

$$SGR = \frac{\sum [(\text{Zone thickness}) \times (\text{Zone clay fraction})]}{\text{Fault throw}} \times 100\%$$
 (5)

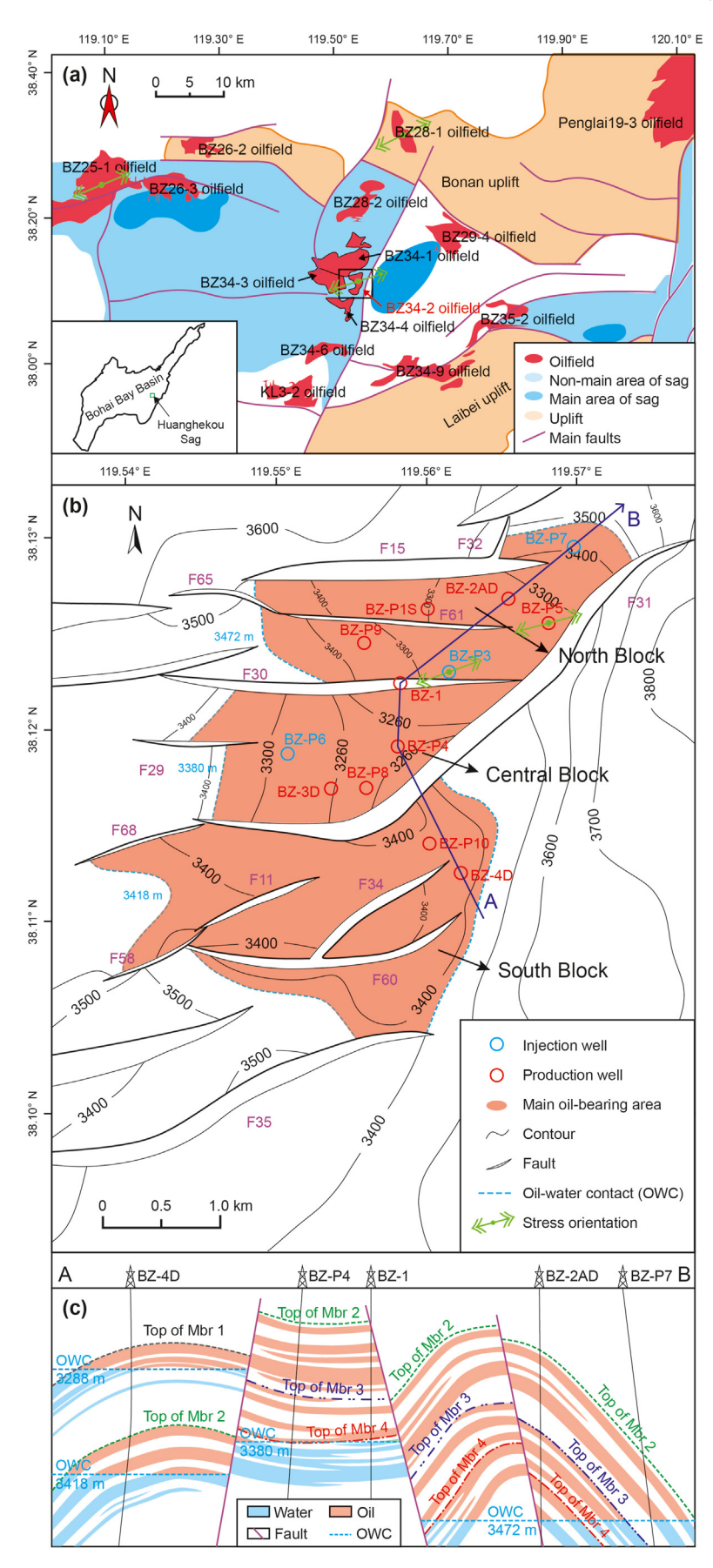
where "Zone clay fraction" is derived from logging interpretation and in the form of volume percentage.

In Eq. (4), the unknown variables σ_n and τ can be calculated based on the interpretation results of in-situ stresses (see section 3.3). Therefore, the most important part is to establish the relationship between the clay content and the friction strength, which can be performed through a large number of experiments, e.g., direct shear (Delle Piane et al., 2016), triaxial friction apparatus (Kohli and Zoback, 2013), and ring shear (Cuisiat and Skurtveit, 2010). Due to the limited availability of core samples, this study uses the data from previous friction strength experiments (Table 1) to characterize the heterogeneity in fault friction strength to illustrate the feasibility of the ECPP and the impact of friction strength heterogeneity on fault stability.

Compared with the clay weight, the friction coefficient of claysand mixtures is more closely related to the clay volume (Osipov, 2011). Therefore, the volume percentage is more significant, which is also consistent with the physical meaning of the SGR. During hydration, clay minerals exhibit a property of decreasing density. Adsorption of water molecules on the internal basal surfaces will increase the distance between structural layers, resulting in intracrystal swelling and volume increase. A previous study showed that the density of smectite group minerals decreases by approximately 25% when wetted compared with the density in the nonhydrated state (Takahashi et al., 2007). However, kaolinites and illite have less effect on intracrystal swelling (Osipov, 2011), so the weight and volume percentages are very close. Only the data from Tembe et al. (2010) and Crawford et al. (2008) are weight percentages in Table 1. Clay minerals include kaolinites, illite and montmorillonite, of which montmorillonite needs to be converted to volume percentage. The densities of saturated montmorillonite and quartz are approximately 2.1 g/cm³ (Takahashi et al., 2007) and 2.64 g/cm³, respectively, according to which the calculation of volume percentage is performed. Data from Logan and Rauenzahn (1987), Brown et al. (2003) and Crawford et al. (2008) are obtained by using GetData software to read the scatter plot of the original paper, which may have minor errors.

3.3. Determination of the in-situ stress

It is often assumed that in-situ stress can be expressed by the vertical stress, maximum horizontal principal stress, and minimum horizontal principal stress under the ground. In addition, their effective stresses are related to pore fluid pressure. The vertical stress can be calculated by bulk density logs. For horizontal stress, the most reliable method is direct measurement, e.g., LOTs (leak-off tests), XLOTs (extended leak-off tests) (Gaarenstroom et al., 1993), HF (hydraulic fracturing), and HTPF (hydraulic testing of preexisting fractures) (Haimson and Cornet, 2003). Unfortunately, these tests are not widely performed during exploration drilling, and only a small amount of XLOT data in neighboring areas can be referenced. At the same time, the Huang model, a pore elastic method mainly using dipole sonic data to calculate the horizontal stress (Huang, 1984), is used to obtain continuous stress data. The key parameter, the tectonic stress coefficient, needs to be calibrated (see section 3.3.2 for details). Pore pressure can be obtained by direct measurement (such as drillstem tests/DSTs, repeat formation



tests/RFTs and modular formation dynamics tests/MDTs) or indirect prediction from related data, such as seismic data (Pennebaker, 1968; Guerra et al., 2019), well logging data (Eaton, 1969; Tingay et al., 2009) and mud weight data (Mouchet and Mitchell, 1989; Tingay et al., 2013). In this paper, only RFT data are available for the determination of pore fluid pressure.

3.3.1. Stress orientation

The stress orientation can be obtained from wellbore phenomena of borehole breakouts (BOs) and drilling-induced tensile fractures (DIFs) (Zoback et al., 1985; Lai et al., 2018, 2019), focal mechanisms (Michael, 1987), and hydraulic fracturing tests (Haimson and Cornet, 2003). Unfortunately, no relevant data were collected in this study, but a previous study showed that the orientation of $S_{\rm Hmax}$ varies from 64° N to 75° N in the Huanghekou Sag (Xu et al., 2011), with little difference horizontally and vertically (Table 2). In addition, the world stress map (Heidbach et al., 2016) shows that there are two kinds of in-situ stress states near the BZ34-2 Oilfield (Fig. 3): the strike-slip stress regime and the normal faulting stress regime, both of which are derived from focal mechanisms with an orientation close to ENE, which is basically consistent with the statistical results of Xu et al. (2011).

3.3.2. Stress magnitude

The vertical stress is mainly caused by the weight of the overburden, which can be obtained by integrating data from bulk density logs:

$$S_{V} = \rho_{W}gh_{W} + \int_{0}^{h} \rho(h)gdh$$
 (6)

where S_V is the vertical stress; ρ_W is the density of water (1.03 g/cm³ for this study); h_W is the water depth (average depth is 20 m in the study area); $\rho(h)$ is the bulk density as a function of depth; g is the gravitational acceleration constant; and h is the burial depth below sea level. Because wellbore enlargement will lead to a low density, the anomalous data are removed according to the caliper logging data

Log-based algorithms for predicting horizontal stress mainly include two categories, namely, the Eaton model and extended Eaton model. The former only considers the Poisson effect of overburden, while the latter also incorporates the effects of poroelasticity and tectonic loading (e.g., Amadei et al. 1987; Thiercelin and Plumb, 1994). Huang model is one of the extended Eaton models, as shown in Eqs. (7) and (8), where $v_{\rm sta}/(1-v_{\rm sta})(S_v-\alpha p_{\rm p})$ represents the contribution of the Poisson effect from the overburden, and $\beta_{\rm h}(S_v-\alpha p_{\rm p})$ and $\beta_{\rm H}(S_v-\alpha p_{\rm p})$ represent the influence of tectonic stress.

$$S_{\text{hmin}} = \left(\frac{\nu_{\text{sta}}}{1 - \nu_{\text{sta}}} + \beta_{\text{h}}\right) \left(S_{\text{v}} - \alpha p_{\text{p}}\right) + \alpha p_{\text{p}}$$
 (7)

$$S_{\text{Hmax}} = \left(\frac{\nu_{\text{sta}}}{1 - \nu_{\text{sta}}} + \beta_{\text{H}}\right) \left(S_{\text{v}} - \alpha p_{\text{p}}\right) + \alpha p_{\text{p}}$$
 (8)

where S_{v} , S_{hmin} , and S_{Hmax} are the vertical stress, minimum horizontal stress and maximum horizontal stress, respectively; ν_{sta} is the static Poisson's ratio, which can be obtained through dynamic

Poisson's ratio conversion; β_h and β_H are the tectonic stress coefficients in the directions of S_{hmin} and S_{Hmax} , respectively; p_p is the pore pressure; and α is the Biot coefficient. The Poisson's ratio, tectonic stress coefficient and Biot coefficient are intermediate parameters, which need to be calculated first.

The calculation of the dynamic Poisson's ratio is performed using dipole sonic log data and density log data according to the following equations:

$$\nu_{\rm dyn} = \frac{0.5\Delta t_{\rm s}^2 - \Delta t_{\rm p}^2}{\Delta t_{\rm s}^2 - \Delta t_{\rm p}^2} \tag{9}$$

where $\Delta t_{\rm p}$ is the compressional slowness, $\Delta t_{\rm s}$ is the shear slowness of the formation, and $\nu_{\rm dyn}$ is the dynamic Poisson's ratio. We have followed the empirical relationship (Lin et al., 1998) to estimate the static Poisson's ratio.

The Biot coefficient is a mechanical property of porous elastic materials that reflects the contribution of pore pressure to the stress of the material skeleton in porous elastic media. The calculation method is shown in Eqs. (10)-(12).

$$C_{\text{ma}} = \frac{3\Delta t_{\text{ms}}^2 \Delta t_{\text{mp}}^2}{\rho_{\text{ma}} \left(3\Delta t_{\text{ms}}^2 - 4\Delta t_{\text{mp}}^2 \right)} \tag{10}$$

$$C_{\rm b} = \frac{3\Delta t_{\rm s}^2 \Delta t_{\rm p}^2}{\rho_{\rm b} \left(3\Delta t_{\rm s}^2 - 4\Delta t_{\rm p}^2\right)} \tag{11}$$

$$\alpha = 1 - \frac{C_{\text{ma}}}{C_{\text{b}}} \tag{12}$$

where ρ_{ma} is the matrix density (2.65 g/cm³ for this study); ρ_{b} is the bulk density of the formation; Δt_{mp} is the compressional slowness of the matrix (333 μ s/m for this study); Δt_{ms} is the shear slowness of the matrix (168 μ s/m for this study); C_{ma} is the compressibility of the matrix; C_{b} is the bulk compressibility; and α is the Biot coefficient.

The tectonic stress coefficients (β_h and β_H) in the direction of the maximum and minimum horizontal stresses need to be inverted from the measured horizontal stress according to Eqs. (6) and (7). Since no HF tests have been performed in the BZ34-2 Oilfield, LOT and XLOT data are used to calculate S_{Hmax} and S_{hmin} (Table 3 and Fig. 4b). The magnitude of S_{hmin} is often represented by the lower envelope of the LOP (leak-off pressure) (Gaarenstroom et al., 1993), while the magnitude of S_{Hmax} can be calculated by the Hubbert—Willis equation (Eq. (13)) under the condition that the tensile strength of the borehole wall is known.

$$S_{\text{Hmax}} = 3S_{\text{hmin}} - FBP - p_{\text{p}} + T \tag{13}$$

where $S_{\rm Hmax}$ and $S_{\rm hmin}$ are the maximum horizontal principal stress and minimum horizontal stress, respectively; *FBP* is the formation breakdown pressure (Fig. 4a); $p_{\rm p}$ is the pore pressure; and T is the tensile strength of the borehole wall.

Fig. 1. (a) The location of the BZ34-2 Oilfield in the Huanghekou Sag, Bohai Bay Basin. (b) Top surface structural map of Mbr 2 in the BZ34-2 Oilfield and oil-bearing area distribution. The deep blue arrow line is the trace of Fig. 1c. (c) Reservoir profile across wells BZ-4D, BZ-94, BZ-1, BZ-2AD and BZ-P7. The South Block has two oil-water contacts (OWCs): the depth of the upper OWC is 3288 m below the surface, and the depth of the lower OWC is 3418 m. The depth of the OWC in the Central Block is 3380 m, and the depth of the OWC in the North Block is 3472 m. The difference in the OWCs indicates that F15, F30, F31, and F32 act as seals for oil in the North and Central Blocks.

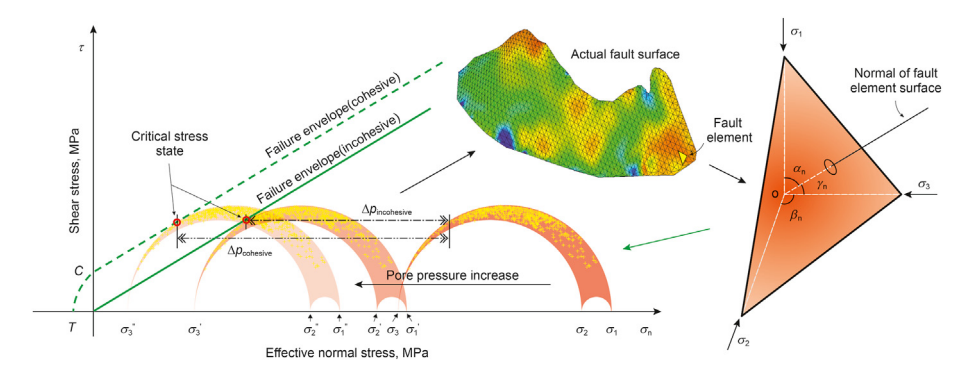


Fig. 2. Schematic diagram of the fault stability evaluation process (modified from Mildren et al., 2005). $\Delta p_{\text{incohesive}}$ represents the risk of cohesionless fault slip, and $\Delta p_{\text{cohesive}}$ represents the risk of cohesive fault slip. The yellow dots represent the stress state of the corresponding fault element, so every element has a value of Δp , which is the horizontal distance from the initial stress state to the critical stress state.

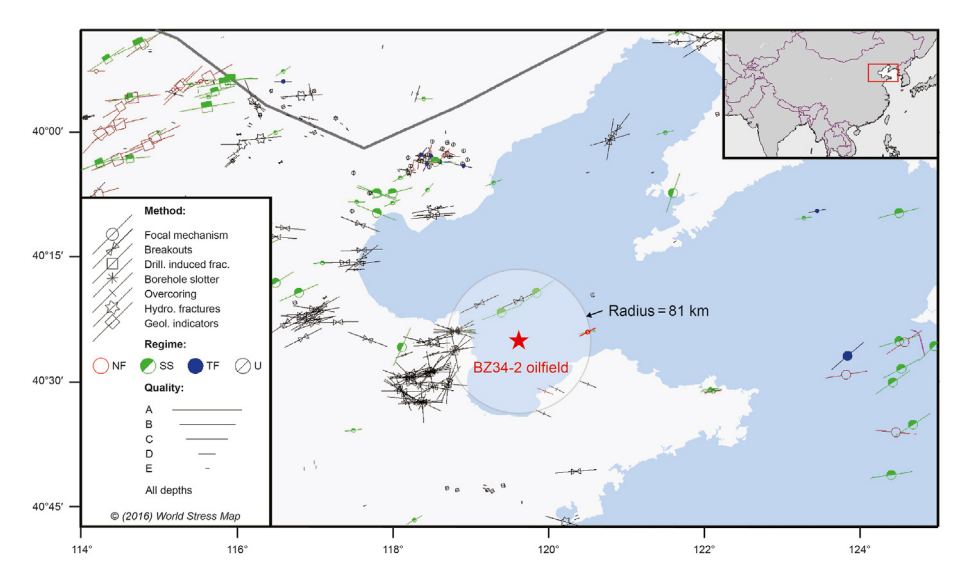


Fig. 3. Excerpt from the World Stress Map (Heidbach et al., 2016) showing the orientation of S_{Hmax} in the BZ34-2 Oilfield and surrounding areas. There are two kinds of stress regimes near the BZ34-2 Oilfield: the strike-slip regime and the normal faulting regime, which are within a radius of 81 km.

4. Results

4.1. Stress orientation and magnitude

The orientations of $S_{\rm Hmax}$ in wells BZ-P3 and BZ-P5 are 70° and 75° , respectively, in the BZ34-2 Oilfield (Table 2), so the average value of 72.5° is used to evaluate the fault stability in this paper. Previous studies have shown that the Shahejie Formation is a normal pressure system with a pressure coefficient (ratio of formation pressure to hydrostatic pressure) between 0.824 and 1.023 (Qi et al., 2005). At the same time, through the measured pressure data of wells BZ-P1S, BZ-2AD and BZ-P5, it is further confirmed that the fluid pressure in the BZ34-2 Oilfield is close to hydrostatic (Fig. 5). The integration of bulk density logs shows that the vertical stress gradient is 19.8-22.5 MPa/km (Fig. 5).

The results of a triaxial compression test at 2800 m in well BZ-1 show that the cohesion C is 19.3 MPa, assuming that the rock failure obeys the composite Griffith—Coulomb failure criterion, whereby T = C/2 = 9.65 MPa. The tensile strength is negligible when there are cohesionless preexisting fractures in the borehole wall and close to intact rock with almost no permeable fractures in the borehole wall. Accordingly, the range of $S_{\rm Hmax}$ at 2800 m is calculated under the assumption that the tensile strength is between 0 and 9.65 MPa, and the results are shown in Table 3 and Fig. 5.

According to this result, the coefficients of tectonic stress β_h and β_H can be inversely calculated with Eqs. (7) and (8). After best fitting, β_h and β_H are 0.288 and 0.502–0.722, respectively. The interpretation result of horizontal stress is shown in the sawtooth line of Fig. 5, which indicates that the stress regime is between the normal faulting stress regime ($S_V > S_{Hmax} > S_{hmin}$) and the transitional stress regime ($S_V \approx S_{Hmax} > S_{hmin}$).

4.2. Risk analysis of fault reactivation under homogeneous friction strength

The stress ratio $\Phi = (S_2 - S_3)/(S_1 - S_3)$ strongly affects the sensitivity of fault stability to variations in strike (Morris and Ferrill, 2009). The closer Φ is to 0.5, the higher the sensitivity of fault stability is to strike. In contrast, the closer the value of Φ is to 0 or 1, the lower the sensitivity of fault stability is to strike. In this study, the uncertainty of S_{Hmax} (S_2), $S_1 = S_v$, is expressed by the change in Φ . According to the interpretation results of S_{Hmax} in section 4.1, the value of Φ is between 0.52 and 1. Within this interval, the sensitivity of fault stability to strike decreases gradually with increasing Φ . It should also be noted that the variation in Φ has no influence on the risk of optimally oriented faults but has a great effect on nonoptimal faults (Morris and Ferrill, 2009). Therefore, this paper uses two boundary values ($S_{\text{Hmax-L}}$ and $S_{\text{Hmax-U}}$) of S_{Hmax} to evaluate the

Table 1
Experimental data statistics of the relationship between the content (volumetric ratio) of different types of clay minerals and the friction coefficient (Lupini et al., 1981; Logan and Rauenzahn, 1987; Brown et al., 2003; Takahashi et al., 2007; Crawford et al., 2008; Tembe et al., 2010).

Mineral mixtures	Total clay volumetric ratio	Friction coefficient	Apparatus	Shear displacement	Shear rate, mm/s	Normal stress $\sigma_{\rm n}/$ confining pressure $p_{\rm c},$ MPa	Water condition	References
Bentonite + quartz	0.00	0.59	Ring shear	Approach	\leq 5.0 \times 10 ⁻³	$0.35 (\sigma_{\rm n})$	Deionized	Lupini et al.
•	0.13	0.59		steady-state	_	,,	water	(1981)
	0.26	0.44		sliding			saturated	
	0.40	0.30						
	0.53	0.12						
	0.66	0.10						
	0.88	0.11						
Montmorillonite + quartz	0.00 0.05	0.51 0.54	Triaxial saw-cut configuration	Approach steady-state	$\begin{array}{c} 1.0\times 10^{-6} \\ -1.0\times 10^{-1} \end{array}$	50 (p _c)	Distilled water saturated	Logan and Rauenzahn
	0.05	0.54	Comiguration	sliding	-1.0 × 10			(1987)
	0.15	0.49		Silding				(1307)
	0.49	0.30						
	0.75	0.15						
	1.00	0.13						
Smectite + quartz	0.00	0.60	Ring shear	Approach	1.5×10^{-3}	1-2 (σ _n)	Seawater	Brown et al.
	0.13	0.58		steady-state			saturated	(2003)
	0.25	0.51		sliding				
	0.37	0.42						
	0.48	0.37						
	0.59	0.25						
	0.69 1.00	0.22 0.10						
Illite + quartz	0.40	0.43	Ring shear	Approach	$\overline{1.5\times10^{-3}}$	<2 (σ _n)	Seawater	Brown et al.
•	0.50	0.36	· ·	steady-state		(11/	saturated	(2003)
	0.60	0.32		sliding				
	0.70	0.26						
	0.99	0.20	_					
${\sf Montmorillonite} + {\sf quartz}$	0.00	0.68	Triaxial saw-cut	2.2 mm	1.2×10^{-3}	75 (effective σ_n)	Distilled water	Takahashi et a
	0.06	0.69	configuration				saturated	(2007)
	0.12	0.60						
	0.18	0.60						
	0.24	0.53						
	0.29	0.48						
	0.35	0.44						
	0.45	0.38						
	0.50	0.30						
	0.55	0.25						
	0.65 0.79	0.19						
	0.79	0.18 0.10						
	1.00	0.10						
Kaolinite + quartz	0.00	0.68	Triaxial saw-cut	5% (shear strain)	$\overline{0.3\times10^{-3}}$	50 (effective p _c)	Distilled water	Crawford et al
	0.00	0.67	configuration			•	saturated	(2008)
	0.10	0.65						
	0.20	0.60						
	0.30	0.51						
	0.30 0.40	0.51 0.45						
	0.30 0.40 0.40	0.51 0.45 0.42						
	0.30 0.40 0.40 0.50	0.51 0.45 0.42 0.43						
	0.30 0.40 0.40 0.50 0.50	0.51 0.45 0.42 0.43 0.42						
	0.30 0.40 0.40 0.50 0.50 1.00	0.51 0.45 0.42 0.43 0.42 0.28	Triaxial saw-cut		1.0 × 10 ⁻³	$\frac{1}{40}$ (effective σ_n)	Dejonized	Tembe et al
oxdot Montmorillonite $+$ quartz	0.30 0.40 0.40 0.50 0.50	0.51 0.45 0.42 0.43 0.42	Triaxial saw-cut configuration	2.3 mm	1.0×10^{-3}	$-\frac{1}{40 \text{ (effective } \sigma_{ m n)}}$	Deionized water	Tembe et al. (2010)
Montmorillonite + quartz	0.30 0.40 0.40 0.50 0.50 1.00 0.00	0.51 0.45 0.42 0.43 0.42 0.28 0.66 0.65		2.3 mm	$\overline{1.0\times10^{-3}}$	$-\frac{1}{40 \ (\text{effective} \ \sigma_{ ext{n}})}$	water	
Montmorillonite + quartz	0.30 0.40 0.40 0.50 0.50 1.00	0.51 0.45 0.42 0.43 0.42 0.28		2.3 mm	1.0×10^{-3}	$-\frac{1}{40 \ (\text{effective} \ \sigma_{ ext{n}})}$		
Montmorillonite + quartz	0.30 0.40 0.40 0.50 0.50 1.00 0.00 0.06 0.18	0.51 0.45 0.42 0.43 0.42 0.28 0.66 0.65 0.63		2.3 mm	1.0 × 10 ⁻³	$-\frac{1}{40~(ext{effective}~\sigma_{ ext{n}})}$	water	
Montmorillonite + quartz	0.30 0.40 0.40 0.50 0.50 1.00 0.00 0.06 0.18 0.30	0.51 0.45 0.42 0.43 0.42 0.28 0.66 0.65 0.63 0.46		2.3 mm	1.0×10^{-3}	$-\frac{1}{40 \text{ (effective } \sigma_{ m n)}}$	water	
Montmorillonite + quartz	0.30 0.40 0.40 0.50 0.50 1.00 0.00 0.06 0.18 0.30 0.56	0.51 0.45 0.42 0.43 0.42 0.28 0.66 0.65 0.63 0.46 0.21		2.3 mm	1.0 × 10 ⁻³	$\frac{1}{40 \ (\text{effective} \ \sigma_{ ext{n}})}$	water	
	0.30 0.40 0.40 0.50 0.50 1.00 0.00 0.06 0.18 0.30 0.56 0.79 1.00 0.00	0.51 0.45 0.42 0.43 0.42 0.28 0.66 0.65 0.63 0.46 0.21 0.16 0.12	configuration Triaxial saw-cut		$\frac{1.0 \times 10^{-3}}{1.0 \times 10^{-3}}$	$\frac{1}{40 \text{ (effective } \sigma_{\text{n}})}$ $\frac{1}{40 \text{ (effective } \sigma_{\text{n}})}$	water saturated Deionized	(2010) Tembe et al.
	0.30 0.40 0.40 0.50 0.50 1.00 0.00 0.06 0.18 0.30 0.56 0.79 1.00 0.00 0.00	0.51 0.45 0.42 0.43 0.42 0.28 0.66 0.65 0.63 0.46 0.21 0.16 0.12 0.66 0.63	configuration				water saturated Deionized water	(2010)
	0.30 0.40 0.40 0.50 0.50 1.00 0.00 0.06 0.18 0.30 0.56 0.79 1.00 0.00 0.05	0.51 0.45 0.42 0.43 0.42 0.28 0.66 0.65 0.63 0.46 0.21 0.16 0.12 0.66 0.63 0.55	configuration Triaxial saw-cut				water saturated Deionized	(2010) Tembe et al.
	0.30 0.40 0.40 0.50 1.00 0.00 0.06 0.18 0.30 0.56 0.79 1.00 0.00 0.015 0.05 0.79	0.51 0.45 0.42 0.43 0.42 0.28 0.66 0.65 0.63 0.46 0.21 0.16 0.12 0.66 0.63 0.44	configuration Triaxial saw-cut				water saturated Deionized water	(2010) Tembe et al.
Montmorillonite + quartz Illite + quartz	0.30 0.40 0.40 0.50 0.50 1.00 0.06 0.18 0.30 0.56 0.79 1.00 0.00 0.15 0.50 0.50 0.88	0.51 0.45 0.42 0.43 0.42 0.28 0.66 0.65 0.63 0.46 0.21 0.16 0.12 0.66 0.63 0.45 0.44	configuration Triaxial saw-cut				water saturated Deionized water	(2010) Tembe et al.
	0.30 0.40 0.40 0.50 1.00 0.00 0.06 0.18 0.30 0.56 0.79 1.00 0.00 0.15 0.25 0.50 0.88 1.00	0.51 0.45 0.42 0.43 0.42 0.28 0.66 0.65 0.63 0.46 0.21 0.16 0.12 0.66 0.63 0.44	configuration Triaxial saw-cut	2.3 mm		40 (effective $\sigma_{\rm n}$)	water saturated Deionized water saturated	(2010) Tembe et al.

(continued on next page)

Table 1 (continued)

Mineral mixtures	Total clay volumetric ratio	Friction Apparatus coefficient	Shear displacement	Shear rate, mm/s	Normal stress $\sigma_{\rm n}/$ confining pressure $p_{\rm c}$, MPa	Water condition	References
	0.38 0.53 0.77 0.95	0.50 0.32 0.20 0.15			-	Deionized water saturated	

Table 2 The orientation of $S_{\rm Hmax}$ in different oilfields in the Huanghekou Sag (Xu et al., 2011), which is obtained from BOs (the orientation of the long axis of BOs is perpendicular to the orientation of $S_{\rm Hmax}$) indicated by the four-arm caliper logs. The oilfield locations are shown in Fig. 1.

Oilfield	Well name	Depth	Orientation of S _{Hmax}
BZ25-1	BZ25-1-2	2013-2042 m	65-70°
BZ25-1	BZ25-1-5	1575-1659 m	70°
BZ25-1	BZ25-1-3	1800-2470 m	65°
BZ28-1	BZ28-1-1	1495-3100 m	64°
BZ34-2	BZ-P3	1968-3180 m	70°
BZ34-2	BZ-P5	1789-1911 m	75°

fault stability (Table 4).

The evaluation results are shown in Figs. 6 and 7. With increasing depth, there is no tangent between Mohr's circle and the failure envelope, and the fault stability is obviously controlled by fault orientation, with faults that have a strike near ENE and a dip angle close to 60° being relatively unstable (Fig. 6). For optimally oriented faults, the Δp is 6.7 MPa at 3100 m and 8.0 MPa at 3500 m under the two boundary conditions of S_{Hmax} (Fig. 6). The Δp of optimally oriented faults increases with depth but is not affected by the change in $S_{\text{Hmax}}(\Phi)$. The projection points of eight faults on the stereogram are close to the optimal faults, and their Δp values range from 5 to 20 MPa. Weak fault segments are located in the middle of fault F30 (point A in Fig. 7) and at the northeastern end of fault F31 (point B in Fig. 7) within Mbr 2 ~ Mbr 4. When $S_{Hmax} = S_{Hmax-I}$, the minimum Δp values are 8.9 MPa (point A) and 9.9 MPa (point B) (Fig. 7a). When $S_{Hmax} = S_{Hmax-U}$, the minimum Δp values are 8.8 MPa (point A) and 9.3 MPa (point B) (Fig. 7b). At point A, with the change in Φ from 0.52 to 1.0, the value of Δp decreases slightly (0.1 MPa), but at point B, it decreases greatly (0.6 MPa). This may be related to the projected position of the risk fault segment on the stereogram: point A is closer to the optimal fault, so the decrease is smaller.

4.3. Risk analysis of fault reactivation considering the heterogeneity of friction strength

As mentioned above, only the influence of clay content within fault zones on the heterogeneity of friction strength is considered in this paper. The friction strength data are shown in Table 1, and the generated scatter plot shows that the relationship between the

friction coefficient and the clay content can be expressed by the tangent function (Fig. 8). However, due to the difference in experimental conditions (such as confining pressure and shear rate) and clay mineral types, the relationship between the friction coefficient and clay content is somewhat discrete. On the whole, montmorillonite has a low friction coefficient, while the friction coefficients of illite and kaolinite are high. Therefore, equations of the upper limit (Eq. (14)), average (Eq. (15)) and lower limit (Eq. (16)) will be used to characterize the heterogeneity of friction strength and the subsequent work of the fault stability evaluation. Eqs. (14)—(16) are fitted by MATLAB software.

$$\mu_1 = 0.1703 \, \text{tan}^{-1} (-7.022 V_{\text{sh}} + 3.131) + 0.5013$$
 (14)

$$\mu_2 = 0.2105 \, \text{tan}^{-1}(-4.609V_{\text{sh}} + 1.834) + 0.4096$$
 (15)

$$\mu_3 = 0.1729 \tan^{-1}(-7.401V_{\rm sh} + 2.971) + 0.3019$$
 (16)

The distribution of SGR in 3-D seismic faults (Fig. 9a) was obtained by the SGR algorithm (Eq. (5)) based on fault throw and logging interpretation of clay content from 13 wells (all wells present in Fig. 1b). The kriging method was used to interpolate the clay content of the host rock between wells. Then, the SGR was transformed into the friction coefficient by Eqs. (14)-(16) (Fig. 9b-d). The results show that the clay content in the eastern part of the fault is higher. Compared with the other layers, Mbr 2 has a higher clay content, and the corresponding friction coefficient is smaller. Finally, basic parameters, such as the friction coefficient, fault strike and dip, in-situ stress ($S_{Hmax} = S_{Hmax-L}$), and pore pressure, were used to calculate Δp (Eqs. (1), (2) and (4)). The results show that the high-risk position corresponds to a low friction coefficient and high SGR (Figs. 9 and 10). A comparison with the results under the condition of $\mu = 0.6$ (Fig. 7) shows that the change in fault stability with depth is more obvious, which is mainly caused by the variation in SGR with depth (Fig. 9). In addition, the strong effect of SGR on fault stability masks the effects of fault orientation, and the high-risk segments of the middle part of F30 (point A) and the northeastern end of F31 (point B) under the condition of $\mu = 0.6$ are no longer obvious (Fig. 10). More obvious high-risk segments are located in F61 and F15 (Fig. 10b). When $\mu=\mu_1(V_{\rm sh})$, the minimum Δp is approximately -2 MPa, corresponding to the fault zone mainly filled with kaolinite and illite clay minerals, and only partial fault segments of F61 and F15 reach the critical stress state. When

Table 3 *LOP, FBP* and interpreted S_{Hmax} (S_{Hmax-L} is the lower limit of S_{Hmax} and S_{Hmax-U} is the upper limit of S_{Hmax}) in the surrounding oilfield.

Oilfield	Well name	TVDSS, m	LOP, MPa	FBP, MPa	S _{Hmax-L} , MPa	S _{Hmax-U} , MPa
BZ34-3	BZ34-3-6	501.5	7.59			
	BZ34-3-5	507	8.16			
BZ34-4	BZ34-4-5	803	13.24			
	BZ34-4-5	2800	44.55	52.64	53.00	62.56
BZ34-1	BZ34-1N-2	507	9.02			
	BZ34-1N-1	503	7.16			

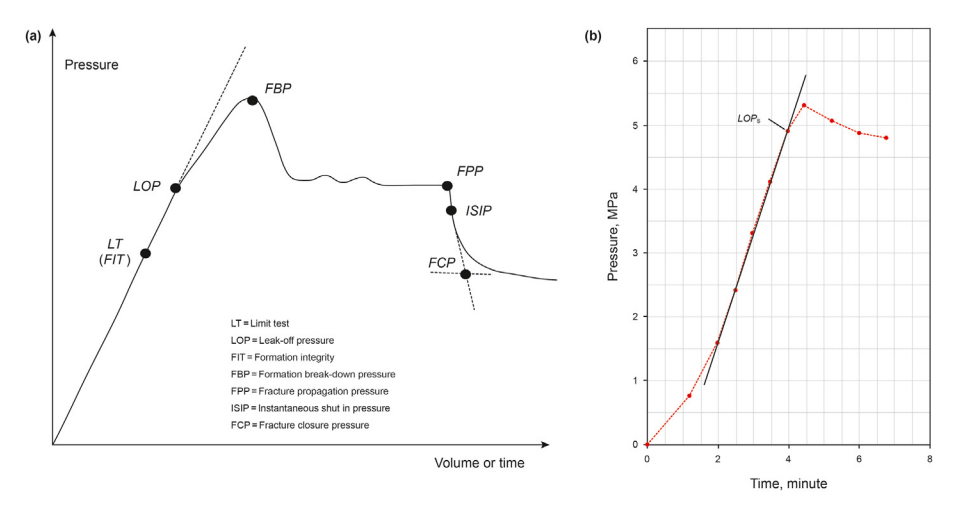


Fig. 4. (a) Idealized relationship between pumping pressure and time or volume of injected fluid during an XLOT (Gaarenstroom et al., 1993). (b) An example of the LOT curve of well BZ34-4-5 at 803 m. The pump pressure is stopped after *LOP*. The *LOP* at the surface (*LOPs*) is 4.89 MPa, which is 13.24 MPa at the bottom hole under a mud weight of 1.06 g/cm³.

 $\mu = \mu_2(V_{\rm sh})$, the minimum Δp is approximately -15 MPa, corresponding to the fault zone mainly filled with kaolinite, illite and montmorillonite mixture, and a small part of fault segments are activated. When $\mu = \mu_3(V_{\rm sh})$, corresponding to the situation in which clay minerals in the fault zone are dominated by montmorillonite, the minimum Δp is approximately -30 MPa, and most fault segments are activated. The contribution of montmorillonite to fault activation has been documented (Numelin et al., 2007; Rolandone et al., 2008; Collettini et al., 2009; Carpenter et al., 2012), and montmorillonite can even cause slip along nonoptimal faults, such as the Zuccale fault (low-angle normal fault) in Elba, Italy (Collettini et al., 2009) and the San Andreas fault with an angle of 70° between the maximum horizontal principal stress and the fault trace in California, USA (Rolandone et al., 2008; Carpenter et al., 2012). Through the comparison of Δp at points A and B under four conditions of friction strength (Fig. 10d), it is found that in the last two cases ($\mu = \mu_2$ and μ_3), $\Delta p < 0$, especially the fault zone dominated by montmorillonite ($\mu = \mu_3$), which fully reflects the necessity of considering the heterogeneity of friction strength.

5. Discussion

A comparison of the results from two cases (Figs. 7 and 10) indicates that the heterogeneity in the fault friction strength is an important factor that affects both the critical pore pressure of faults and the location of risky fault segments. This is of great significance for related fields such as conventional oil and gas development, waste fluid disposal, and gas storage. In the process of characterizing the heterogeneity of fault friction strength, this study uses the published data of friction experiments, which may not be very suitable for this paper because of the difference in clay mineral type and experimental conditions. Therefore, this paper only points out the feasibility of this extended method and the relative risk segment of faults, and there is some uncertainty about the absolute value of the fault stability. In practical applications, it is better to carry out experiments (ring shear, direct shear or triaxial saw-cut tests) under in-situ conditions to generate actual friction data to obtain a more suitable equation for the friction coefficient.

Field measurements of the in-situ stress show that the horizontal stress is highly dependent on lithology (e.g., Warpinski, 1989; Wileveau et al., 2007; Gunzburger and Magnenet, 2014). According to the extended Eaton models (Amadei et al., 1987; Thiercelin and Plumb, 1994), which incorporate the effects of elastic

anisotropy, poroelasticity, and tectonic loading, lithologies with a high Poisson's ratio (such as shale) tend to accommodate high

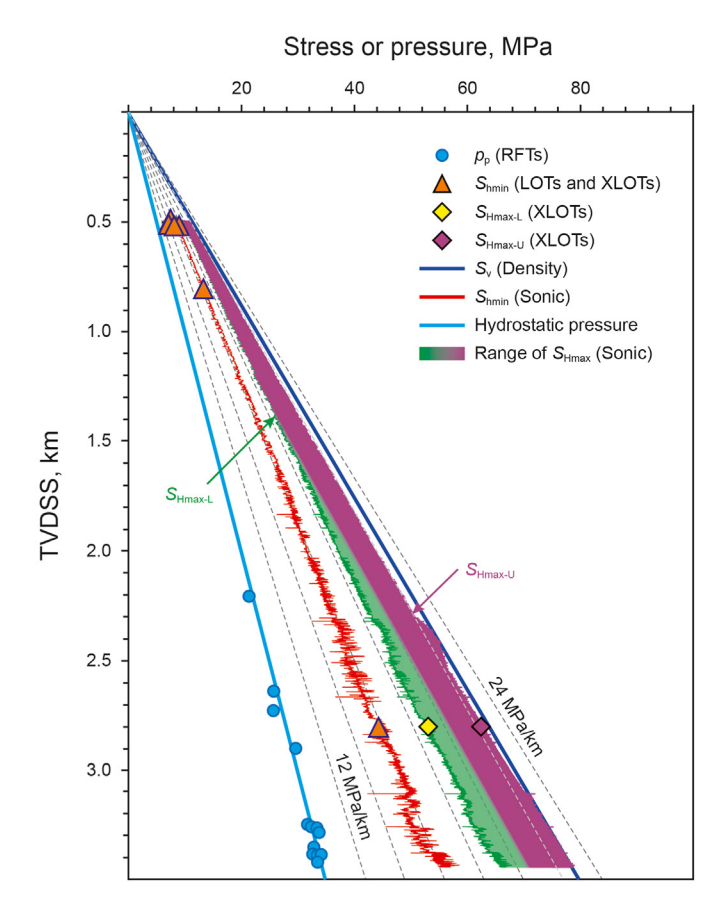


Fig. 5. Vertical distribution of the in-situ stress and pore pressure in the BZ34-2 Oil-field. Pore pressure was obtained from RFT data. According to the horizontal stress calculated from the LOT and XLOT data, the maximum horizontal principal stress is less than or equal to the vertical stress, indicating either a normal faulting $(S_{\rm V} > S_{\rm Hmax} > S_{\rm hmin})$ or transition stress regime $(S_{\rm V} \approx S_{\rm Hmax} > S_{\rm hmin})$ in the BZ34-2 Oilfield. Interpolation mainly uses dipole acoustic data through the Huang model in the well interval without leak-off data, and horizontal stress curves are converted from well BZ-1.

Table 4 Parameter settings for fault stability evaluation.

Input parameter	S _v , MPa	$S_{ m Hmax-I}/S_{ m Hmax-u}$, MPa	S _{hmin} , MPa	$p_{\rm p,}$ MPa	Stress direction, $^{\circ}$	Cohesion, MPa	Friction coefficient
TVDSS, m	3100	3100	3100	3100	72.5	0	0.6
Gradient, MPa/m	0.0248	0.0212/0.0250	0.0171	0.01			
Pressure, MPa	68.71	58.59/68.74	47.61	31			

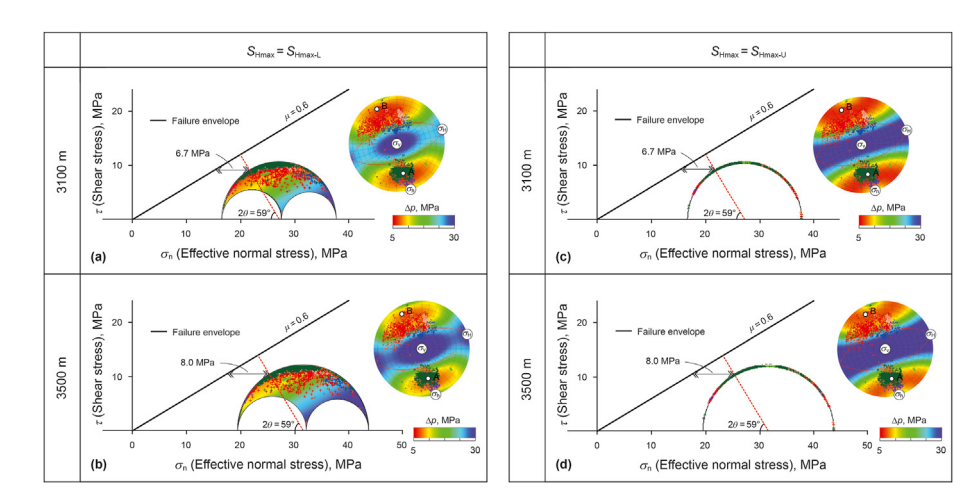


Fig. 6. Mohr diagram and stereogram of Δp using the Coulomb failure envelope of $\mu = 0.6$ at reservoir depths of 3100 m and 3500 m. Red arcs on the stereogram represent two optimal fault orientations ($-17.5^{\circ} \angle 60^{\circ}$ and $162.5^{\circ} \angle 60^{\circ}$) for reactivation. (a) Mohr diagram and stereogram at 3100 m under the condition $S_{Hmax} = S_{Hmax-L}$; (b) Mohr diagram and stereogram at 3500 m under the condition $S_{Hmax} = S_{Hmax-L}$; (c) Mohr diagram and stereogram at 3500 m under the condition $S_{Hmax} = S_{Hmax-U}$; (d) Mohr diagram and stereogram at 3500 m under the condition $S_{Hmax} = S_{Hmax-U}$. The cross points of different colors are projection points of 8 faults on the stereogram, and A and B are normal projections of fault elements A and B in Fig. 7.

stresses in a normal stress regime ($S_V > S_{Hmax} > S_{hmin}$). The horizontal stress is mainly governed by the component from the Poisson effect of the overburden, so the adjacent stiff sandstone normally has a lower horizontal stress. Conversely, in reverse ($S_{Hmax} > S_V > S_{hmin}$) and strike-slip ($S_{Hmax} > S_{hmin} > S_V$) stress regimes, the horizontal stress is mainly governed by the tectonic component, and stiff sandstone will accommodate high stresses, so the adjacent compliant shale normally has a lower horizontal stress. In addition, viscoelastic stress relaxation can also cause stress changes in interbedded layers (Gunzburger and Cornet, 2007; Sone and Zoback, 2014), and the overall effect is to make a stress state move toward the isotropic state. Therefore, it is equally important to investigate the dependence of stress on lithology or clay content to improve the accuracy of fault stability evaluation.

According to previous research (Shimamoto and Logan, 1981; Morrow et al., 2000; Saffer and Marone, 2003; Anthony and Marone, 2005; Takahashi et al., 2007; Moore and Lockner, 2008; Tembe et al., 2010; Behnsen and Faulkner, 2012; Haines et al., 2013; Bullock et al., 2015), the factors influencing fault friction strength can be divided into two categories: intrinsic and extrinsic factors. The intrinsic factors mainly include the particle characteristics and the type and content of clay minerals; the extrinsic factors mainly include effective normal stress, wetness and temperature. For a reservoir with little change in depth, the extrinsic factors do not change much and can be set to a fixed value during experiments. For instance, the depth difference of the Shahejie Formation in this study is approximately 500 m, the change in effective normal stress is within 12 MPa, and the change in temperature is approximately

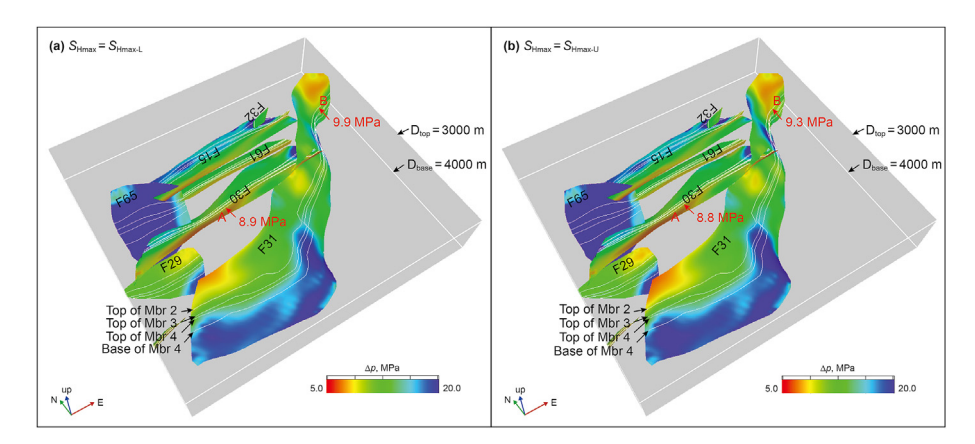


Fig. 7. (a) Distribution of Δp on 3-D seismic faults under the condition of $S_{Hmax} = S_{Hmax-L}$. Risk segments of the fault are located in the middle of F30 and the northeastern end of fault F31 at the top of E3s1-2, and Δp is 8.9 MPa (point A) and 9.9 MPa (point B); (b) Distribution of Δp on 3-D seismic faults under the condition $S_{Hmax} = S_{Hmax-u}$, and Δp is 8.8 MPa (point A) and 9.3 MPa (point B).

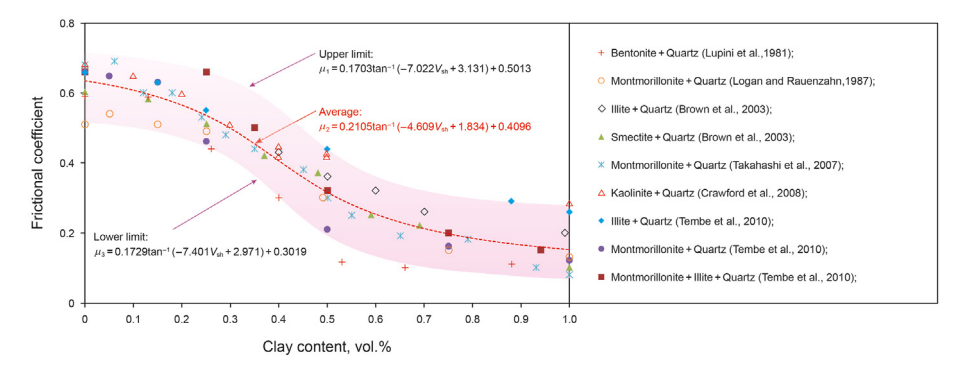


Fig. 8. The relationship between the clay content and the friction strength (detailed data shown in Table 1).

15 °C. According to the results from Saffer and Marone (2003) and Zhang and He (2013), the change in the friction coefficient is very small, within 0.02. However, in the case of faults developed in reservoirs with a large vertical extent and thermal recovery, it is necessary to take all factors into account as much as possible, which is very large work. A feasible idea is to build a shareable cloud database to collect a large amount of data in a short time. Then, machine learning can be used to study the comprehensive expression of friction strength applicable to different geological conditions, which is our future work.

6. Conclusions

An extended evaluation method (ECPP) of fault stability incorporating the heterogeneity in friction strength caused by variation in the clay content within fault zones has been established here.

The basic steps are as follows: first, the distribution of SGR on 3-D seismic faults is calculated based on logging interpretation of clay content and fault throw data; then, the relationship between the friction coefficient and SGR/V_{sh} is obtained through a large number of experiments; and finally, the friction coefficient is integrated into the Coulomb failure criterion as a function of SGR to calculate the critical pore pressure of faults.

The in-situ stress was determined by incorporating data available from core measurements, well logging and well testing data from boreholes. The stress regime is between $S_{\rm V} > S_{\rm Hmax} > S_{\rm hmin}$ and $S_{\rm V} \approx S_{\rm Hmax} > S_{\rm hmin}$ with $S_{\rm Hmax}$ oriented ENE. Based on the interpretation results of in-situ stress, both methods were employed to investigate the stability of faults. The traditional evaluation result of fault stability shows that all faults are stable. The relatively risky fault segments are located in the middle of fault F30 and on the northeastern end of fault F31 within the top of Mbr 2, and the

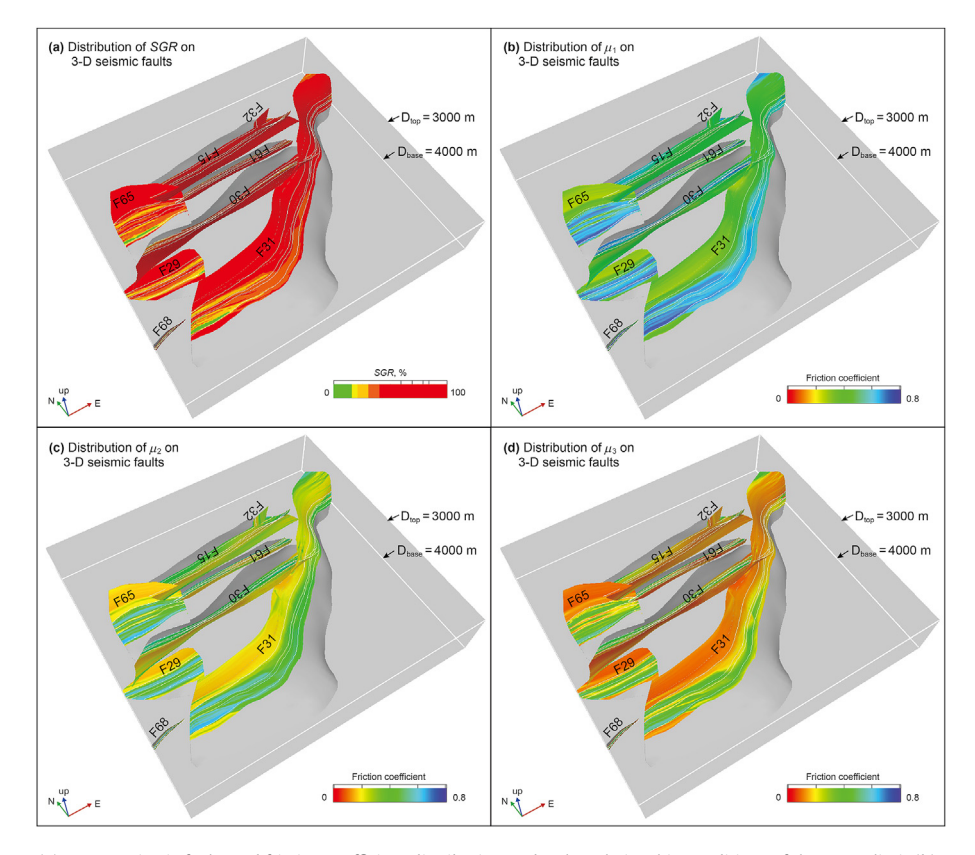


Fig. 9. The distribution of SGR (a) on 3-D seismic faults and friction coefficient distribution under the relationship conditions of the upper limit (b), average (c) and lower limit (d).

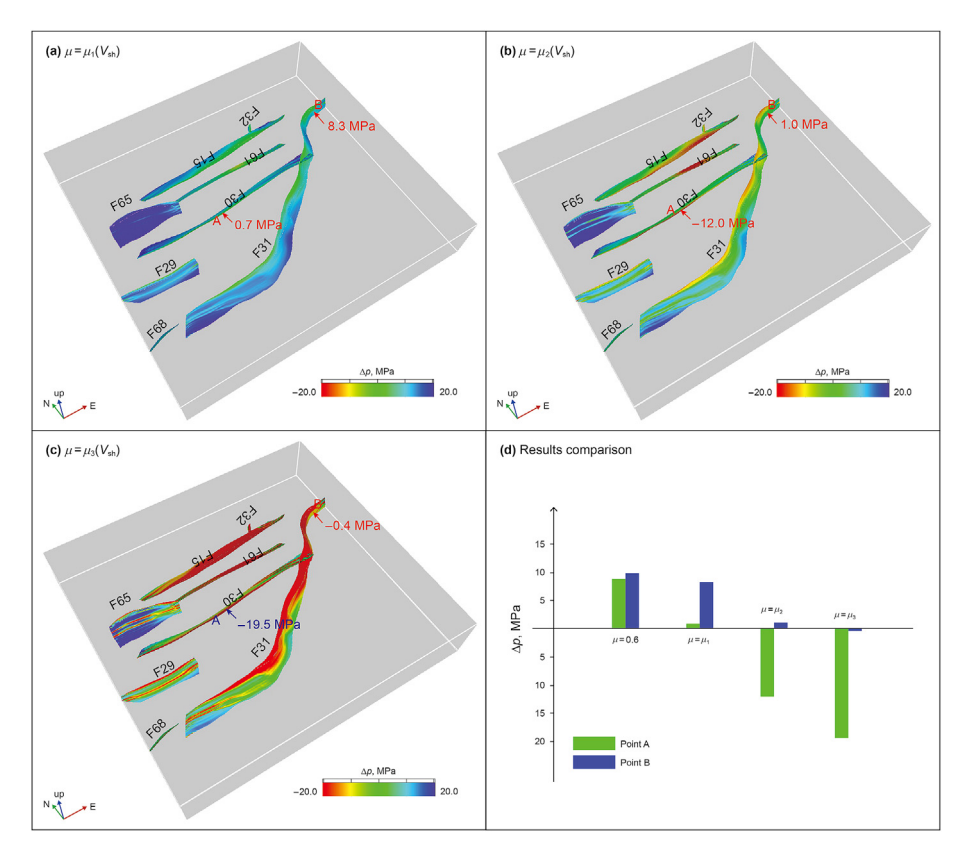


Fig. 10. The distribution of Δp on 3-D seismic faults within Mbr2 ~ Mbr4 under conditions of the upper limit (a), average (b) and lower limit (c) relationships of the friction coefficient. (d) Results comparison of Δp at points A and B under three conditions.

maximum sustainable fluid pressure Δp of these segments is approximately 8.8–8.9 MPa and 9.3–9.9 MPa, respectively. When considering the heterogeneity of fault friction strength, the Δp value is clearly controlled by the clay content of faults, and risky fault segments such as F30 and F31 assessed using traditional methods are no longer obvious, which reflects the importance of incorporating friction strength heterogeneity in the process of fault evaluation. It is worth noting that in some cases, the friction strength is clearly controlled by multiple factors. Future work should focus on establishing a database through a large number of experiments and investigating the relationship between the friction coefficient and variables by machine learning.

Statements and declarations

We declare that we have no known competing financial interests or personal relationships that could have appeared to influence the work reported in this paper.

Acknowledgements

The authors greatly appreciate the financial support from the National Natural Science Foundation of China (Grant Nos. 42002152 and U20A2093) and National Key Research and Development Program of China (Grant No. 2022YFE0206800). We are grateful to FAPS Energy Technology Ltd. (www.faps.com.cn) for the use of FAPSeal software.

References

Allen, M.B., Macdonald, D.I.M., Xun, Z., et al., 1997. Early Cenozoic two-phase extension and late Cenozoic thermal subsidence and inversion of the Bohai

Basin, northern China. Mar. Petrol. Geol. 14 (7–8), 951–972. https://doi.org/10.1016/s0264-8172(97)00027-5.

Amadei, B., Savage, W.Z., Swolfs, H.S., 1987. Gravitational stresses in anisotropic rock masses. Int. J. Rock Mech. Min. Sci. Geomech. Abstr. 24 (1), 5–14. https://doi.org/10.1016/0148-9062(87)91227-7.

Amiri, M., Lashkaripour, G.R., Ghabezloo, S., et al., 2019. Mechanical earth modeling and fault reactivation analysis for CO₂-enhanced oil recovery in Gachsaran oil field, south-west of Iran. Environ. Earth Sci. 78 (4), 1–22. https://doi.org/ 10.1007/s12665-019-8062-1.

Anthony, J.L., Marone, C., 2005. Influence of particle characteristics on granular friction. J. Geophys. Res. Solid Earth 110 (B8), 1–14. https://doi.org/10.1029/2004|B003399.

Behnsen, J., Faulkner, D.R., 2012. The effect of mineralogy and effective normal stress on frictional strength of sheet silicates. J. Struct. Geol. 42, 49–61. https://doi.org/10.1016/j.jsg.2012.06.015.

Brown, K.M., Kopf, A., Underwood, M.B., et al., 2003. Compositional and fluid pressure controls on the state of stress on the Nankai subduction thrust: a weak plate boundary. Earth Planet Sci. Lett. 214 (3–4), 589–603. https://doi.org/10.1016/S0012-821X(03)00388-1.

Bullock, R.J., de Paola, N., Holdsworth, R.E., 2015. An experimental investigation into the role of phyllosilicate content on earthquake propagation during seismic slip in carbonate faults. J. Geophys. Res. Solid Earth 120 (5), 3187–3207. https://doi.org/10.1002/2015JB011914.

Carpenter, B.M., Saffer, D.M., Marone, C., 2012. Frictional properties and sliding stability of the San Andreas fault from deep drill core. Geology 40 (8), 759–762. https://doi.org/10.1130/G33007.1.

Castillo, D.A., Bishop, D.J., Donaldson, I., et al., 2000. Trap integrity in the laminaria high-Nancar trough region, Timor Sea: prediction of fault seal failure using well-constrained stress tensors and fault surfaces interpreted from 3d seismic. APPEA J. 40 (1), 151–173. https://doi.org/10.1071/aj99009.

Cesca, S., Grigoli, F., Heimann, S., et al., 2014. The 2013 September-October seismic sequence offshore Spain: a case of seismicity triggered by gas injection? Geophys. J. Int. 198 (2), 941–953. https://doi.org/10.1093/gji/ggu172.

Collettini, C., Viti, C., Smith, S.A.F., et al., 2009. Development of interconnected talc networks and weakening of continental low-angle normal faults. Geology 37 (6), 567–570. https://doi.org/10.1130/G25645A.1.

Crawford, B.R., Faulkner, D.R., Rutter, E.H., 2008. Strength, porosity, and permeability development during hydrostatic and shear loading of synthetic quartz-clay fault gouge. J. Geophys. Res. Solid Earth 113 (B3), 1–14. https://doi.org/10.1029/2006JB004634.

Cuisiat, F., Skurtveit, E., 2010. An experimental investigation of the development

Y.-J. Jin, L.-D. Meng, D.-Y. Lyu et al. Petroleum Science 20 (2023) 2695–2708

and permeability of clay smears along faults in uncemented sediments. J. Struct. Geol. 32 (11), 1850–1863. https://doi.org/10.1016/j.jsg.2009.12.005.

- Delle Piane, C., Giwelli, A., Clennell, M. ben, et al., 2016. Frictional and hydraulic behaviour of carbonate fault gouge during fault reactivation an experimental study. Tectonophysics 690, 21–34. https://doi.org/10.1016/j.tecto.2016.07.011.
- Dusseault, M.B., Bruno, M.S., Barrera, J., 2001. Casing shear: causes, cases, cures. SPE Drill. Complet. 16 (2), 98–107. https://doi.org/10.2118/72060-PA.
- Eaton, B.A., 1969. Fracture gradient prediction and its application in oilfield operations. J. Petrol. Technol. 21 (10), 1353—1360.
- Ellsworth, W.L., 2013. Injection-induced earthquakes. Science 341 (6142), 1225942. https://doi.org/10.1126/science.1225942.
- Ferrill, D.A., Winterle, J., Wittmeyer, G., et al., 1999. Stressed rock strains ground-water at Yucca Mountain, Nevada. GSA Today 9 (5), 1–8. Gaarenstroom, L., Tromp, R.A.J., de Jong, M.C., et al., 1993. Overpressures in the
- Gaarenstroom, L., Tromp, R.A.J., de Jong, M.C., et al., 1993. Overpressures in the central north sea: implications for trap integrity and drilling safety. Petrol. Geol. Conf. Proc. 4 (1), 1305–1313. https://doi.org/10.1144/0041305.
- Gamboa, D., Williams, J.D.O., Bentham, M., et al., 2019. Application of three-dimensional fault stress models for assessment of fault stability for CO₂ storage sites. Int. J. Greenh. Gas Control 90, 102820. https://doi.org/10.1016/j.ijggc.2019.102820.
- Gan, W., Frohlich, C., 2013. Gas injection may have triggered earthquakes in the Cogdell oil field, Texas. Proc. Natl. Acad. Sci. U.S.A. 110 (47), 18786–18791. https://doi.org/10.1073/pnas.1311316110.
- Guerra, C., Fischer, K., Henk, A., 2019. Stress prediction using 1D and 3D geomechanical models of a tight gas reservoir—a case study from the Lower Magdalena Valley Basin, Colombia. Geomech. Energy Environ. 19, 100113. https://doi.org/10.1016/j.gete.2019.01.002.
- Gunzburger, Y., Cornet, F.H., 2007. Rheological characterization of a sedimentary formation from a stress profile inversion. Geophys. J. Int. 168 (1), 402–418. https://doi.org/10.1111/j.1365-246X.2006.03140.x.
- Gunzburger, Y., Magnenet, V., 2014. Stress inversion and basement-cover stress transmission across weak layers in the Paris basin, France. Tectonophysics 617, 44–57. https://doi.org/10.1016/j.tecto.2014.01.016.
- Haimson, B.C., Cornet, F.H., 2003. ISRM suggested methods for rock stress estimation-part 3: hydraulic fracturing (HF) and/or hydraulic testing of pre-existing fractures (HTPF). Int. J. Rock Mech. Min. 40 (7–8), 1011–1020. https://doi.org/10.1016/j.ijrmms.2003.08.002.
- Haines, S.H., Kaproth, B., Marone, C., et al., 2013. Shear zones in clay-rich fault gouge: a laboratory study of fabric development and evolution. J. Struct. Geol. 51, 206–225. https://doi.org/10.1016/j.jsg.2013.01.002.
- Hao, F., Zhou, X., Zhu, Y., et al., 2010. Charging of oil fields surrounding the Shaleitian uplift from multiple source rock intervals and generative kitchens, Bohai Bay basin, China. Mar. Petrol. Geol. 27 (9), 1910–1926. https://doi.org/10.1016/j.marpetgeo.2010.07.005.
- Healy, J.H., Rubey, W.W., Griggs, D.T., et al., 1968. The Denver earthquakes. Science 161 (3848) 1301—1310. https://doi.org/10.1126/science.161.3848.1301
- 161 (3848), 1301—1310. https://doi.org/10.1126/science.161.3848.1301.

 Heidbach, O., Rajabi, M., Reiter, K., et al., 2016. World Stress Map Database Release 2016. GFZ Data Services 10. http://doi.org/10.5880/WSM.2016.001.
- Hellebrekers, N., Niemeijer, A.R., Fagereng, Å., et al., 2019. Lower crustal earthquakes in the East African Rift System: insights from frictional properties of rock samples from the Malawi rift. Tectonophysics 767, 228167. https://doi.org/ 10.1016/j.tecto.2019.228167.
- Hsiao, L.Y., Graham, S.A., Tilander, N., 2004. Seismic reflection imaging of a major strike-slip fault zone in a rift system: Paleogene structure and evolution of the Tan-Lu fault system, Liaodong Bay, Bohai, offshore China. AAPG Bull. 88 (1), 71–97. https://doi.org/10.1306/09090302019.
- Hu, X., Zang, A., Heidbach, O., et al., 2017. Crustal stress pattern in China and its adjacent areas. J. Asian Earth Sci. 149, 20–28. https://doi.org/10.1016/ j.jseaes.2017.07.005.
- Huang, R., 1984. A model for predicting formation fracture pressure. J. Univ. Pet., China (Ed. Nat. Sci.) 26 (4), 335–347.
- Jaeger, J.C., Cook, N.G.W., 1979. Fundamentals of Rock Mechanics, third ed. Chapman and Hall, London.
- Kaven, J.O., Hickman, S.H., McGarr, A.F., et al., 2015. Surface monitoring of microseismicity at the Decatur, Illinois, CO2 sequestration demonstration site. Seismol Res. Lett. 86 (4), 1096–1101. https://doi.org/10.1785/0220150062.
- Knipe, R.J., Fisher, Q.J., Jones, G., et al., 1997. Fault Seal Analysis: Successful Methodologies, Application and Future Directions, vol. 7. Norwegian Petroleum Society Special Publications, pp. 15–38. https://doi.org/10.1016/S0928-8937(97)80004.5
- Kohli, A.H., Zoback, M.D., 2013. Frictional properties of shale reservoir rocks. J. Geophys. Res. Solid Earth 118 (9), 5109-5125. https://doi.org/10.1002/jgrb.50346.
- Lai, J., Li, D., Wang, G., et al., 2019. Earth stress and reservoir quality evaluation in high and steep structure: the Lower Cretaceous in the Kuqa Depression, Tarim Basin, China. Mar. Petrol. Geol. 101, 43–54. https://doi.org/10.1016/ j.marpetgeo.2018.11.036.
- Lai, J., Wang, G., Wang, S., et al., 2018. A review on the applications of image logs in structural analysis and sedimentary characterization. Mar. Petrol. Geol. 95, 139–166. https://doi.org/10.1016/j.marpetgeo.2018.04.020.
- Langhi, L., Zhang, Y., Gartrell, A., et al., 2010. Evaluating hydrocarbon trap integrity during fault reactivation using geomechanical three-dimensional modeling: an example from the Timor Sea, Australia. AAPG Bull. 94 (4), 567–591. https:// doi.org/10.1306/101309909046.
- Leclère, H., Calais, É., 2019. A parametric analysis of fault reactivation in the new

- madrid seismic zone: the role of pore fluid overpressure. J. Geophys. Res. Solid Earth 124 (10), 10630—10648. https://doi.org/10.1029/2018/B017181.
- Lin, Y., Ge, H., Wang, S., 1998. Testing study on dynamic and static elastic parameters of rocks. Chin. J. Rock Mech. Eng. 17 (2), 216–222.
- Liu, X., Xi, S., 2012. Analysis on the geological genesis of marine oil spill: a case study of Penglai 19-3 oilfield, bohai Bay Basin. Mar. Inf. 27 (3), 1-7.
- Logan, J.M., Rauenzahn, K.A., 1987. Frictional dependence of gouge mixtures of quartz and montmorillonite on velocity, composition and fabric. Tectonophysics 144 (1–3), 87–108. https://doi.org/10.1016/0040-1951(87)90010-2.
- Lupini, J.F., Skinner, A.E., Vaughan, P.R., 1981. The drained residual strength of cohesive soils. Géotechnique 31 (2), 181–213.
- Manga, M., Wang, C.Y., Shirzaei, M., 2016. Increased stream discharge after the 3 September 2016 Mw 5.8 Pawnee, Oklahoma earthquake. Geophys. Res. Lett. 43 (22), 11–588. https://doi.org/10.1002/2016GL071268.
- Mao, L., Tian, J., Wang, L., et al., 2019. Initiation and origin of dextral deformation at mid-eocene in the western bohai Bay Basin, east China. J. Asian Earth Sci. 185, 104031. https://doi.org/10.1016/j.jseaes.2019.104031.
- Mao, L., Zhao, X., Zhang, S., et al., 2021. Structures and kinematics of the huanghua depression in bohai bay basin, east China: implications for the formation mechanism of a transtensional basin. Lithosphere 2021 (1), 6637416. https://doi.org/10.2113/2021/6637416.
- McGarr, A., Barbour, A.J., 2017. Wastewater disposal and the earthquake sequences during 2016 near fairview, Pawnee, and cushing, Oklahoma. Geophys. Res. Lett. 44 (18), 9330–9336. https://doi.org/10.1002/2017GL075258.
- Meng, L., Fu, X., Lv, Y., et al., 2017. Risking fault reactivation induced by gas injection into depleted reservoirs based on the heterogeneity of geomechanical properties of fault zones. Petrol. Geosci. 23 (1), 29–38. https://doi.org/10.1144/petgeo2016-031.
- Michael, A.J., 1987. Use of focal mechanisms to determine stress: a control study. J. Geophys. Res. 92 (B1), 357–368. https://doi.org/10.1029/JB092iB01p00357.
- Mildren, S.D., Hillis, R.R., Lyon, P.J., et al., 2005. FAST: a new technique for geomechanical assessment of the risk of reactivation-related breach of fault seals. In: Boult, P., Kaldi, J. (Eds.), Evaluating Fault and Cap Rock Seals: AAPG Hedberg Series, vol. 2, pp. 73–85. https://doi.org/10.1306/1060757H23163.
- Mohammed, A.I., Oyeneyin, B., Atchison, B., et al., 2019. Casing structural integrity and failure modes in a range of well types a review. J. Nat. Gas Sci. Eng. 68, 102898. https://doi.org/10.1016/j.jngse.2019.05.011.
- Moore, D.E., Lockner, D.A., 2008. Talc friction in the temperature range 25-400°C: relevance for fault-zone weakening. Tectonophysics 449 (1–4), 120–132. https://doi.org/10.1016/j.tecto.2007.11.039.
- Morris, A., Ferrill, D.A., Henderson, D.B., 1996. Slip-tendency analysis and fault reactivation. Geology 24 (3), 275–278. https://doi.org/10.1130/0091-7613(1996) 024<0275:STAAFR>2.3.CO:2.
- Morris, A.P., Ferrill, D.A., 2009. The importance of the effective intermediate principal stress (σ'2) to fault slip patterns. J. Struct. Geol. 31 (9), 950–959. https://doi.org/10.1016/j.jsg.2008.03.013.
- Morrow, C.A., Moore, D.E., Lockner, D.A., 2000. The effect of mineral bond strength and adsorbed water on fault gouge frictional strength. Geophys. Res. Lett. 27 (6), 815–818. https://doi.org/10.1029/1999GL008401.
- Mouchet, J.P., Mitchell, A., 1989. Abnormal Pressures while Drilling: Origins, Prediction, Detection, Evaluation. Editions Technip.
- Numelin, T.J., Marone, C., Kirby, E., 2007. Frictional properties of natural fault gouge from a low-angle normal fault, Panamit Valley, California. Tectonics 26 (2), 1–14. https://doi.org/10.1029/2005TC001916.
- Osipov, V.I., 2011. Density of clay minerals. Soil Mech. Found. Eng. 48 (6), 231–240. https://doi.org/10.1007/s11204-012-9153-0.
- Pei, Y., Paton, D.A., Knipe, R.J., et al., 2015. A review of fault sealing behaviour and its evaluation in siliciclastic rocks. Earth Sci. Rev. 150, 121–138. https://doi.org/ 10.1016/j.earscirev.2015.07.011.
- Pennebaker, E.S., 1968. Seismic data indicate depth, magnitude of abnormal pressure. World Oil 166, 73–77.
- Qi, H.Z., Pan, Y.Y., Qiu, Z.W., et al., 2005. Analysis and application of hole instability in well BZ34-2-P1S. Natural Gas Exploration and Development 28 (3), 66–68 (in Chipese)
- Qi, J., Yang, Q., 2010. Cenozoic structural deformation and dynamic processes of the Bohai Bay basin province, China. Mar. Petrol. Geol. 27 (4), 757–771. https:// doi.org/10.1016/j.marpetgeo.2009.08.012.
- Raleigh, C.B., Healy, J.H., Bredehoeft, J.D., 1976. An experiment in earthquake control at Rangely, Colorado. Science 191 (4233), 1230–1237. https://doi.org/10.1126/science.191.4233.1230.
- Rolandone, F., Bürgmann, R., Agnew, D.C., et al., 2008. Aseismic slip and faultnormal strain along the central creeping section of the San Andreas fault. Geophys. Res. Lett. 35 (14), L14305. https://doi.org/10.1029/2008GL034437.
- Saffer, D.M., Marone, C., 2003. Comparison of smectite- and illite-rich gouge frictional properties: application to the updip limit of the seismogenic zone along subduction megathrusts. Earth Planet Sci. Lett. 215 (1–2), 219–235. https://doi.org/10.1016/S0012-821X(03)00424-2.
- Schwab, D.R., Bidgoli, T.S., Taylor, M.H., 2017. Characterizing the potential for injection-induced fault reactivation through subsurface structural mapping and stress field analysis, wellington field, Sumner county, Kansas. J. Geophys. Res. Solid Earth 122 (12), 10132–10154. https://doi.org/10.1002/2017/B014071.
- Shimamoto, T., Logan, J.M., 1981. Effects of simulated clay gouges on the sliding behavior of Tennessee sandston. Tectonophysics 75 (3–4), 243–255. https://doi.org/10.1016/0040-1951(81)90276-6.
- Sibson, R.H., 2017. The edge of failure: critical stress overpressure states in different

- tectonic regimes. Geol. Soc. Spec. Publ. 458 (1), 131–141. https://doi.org/10.1144/SP458.5
- Sone, H., Zoback, M.D., 2014. Viscous relaxation model for predicting least principal stress magnitudes in sedimentary rocks. J. Pet. Sci. Eng. 124, 416–431. https:// doi.org/10.1016/j.petrol.2014.09.022.
- Streit, J.E., 1999. Conditions for earthquake surface rupture along the San Andreas fault system, California. J. Geophys. Res. Solid Earth 104 (B8), 17929–17939. https://doi.org/10.1029/1999jb900131.
- Summers, R., Byerlee, J., 1977. A note on the effect of fault gouge composition on the stability of frictional sliding. Int. J. Rock Mech. Min. Sci. Geomech. Abstr. 14 (3), 155–160. https://doi.org/10.1016/0148-9062(77)90007-9.
- Sun, H., Zhou, X., Peng, W., et al., 2011. Late-stage hydrocarbon accumulation and enrichment in the Huanghekou Sag, southern bohai sea. Petrol. Explor. Dev. 38 (3), 307–313.
- Taghipour, M., Ghafoori, M., Lashkaripour, G.R., et al., 2019. Estimation of the current stress field and fault reactivation analysis in the Asmari reservoir, SW Iran. Petrol. Sci. 16 (3), 513–526. https://doi.org/10.1007/s12182-019-0331-9.
- Petrol. Sci. 16 (3), 513–526. https://doi.org/10.1007/s12182-019-0331-9.

 Takahashi, M., Mizoguchi, K., Kitamura, K., et al., 2007. Effects of clay content on the frictional strength and fluid transport property of faults. J. Geophys. Res. Solid Earth 112 (B8), 1–12. https://doi.org/10.1029/2006/B004678.
- Tembe, S., Lockner, D.A., Wong, T.F., 2010. Effect of clay content and mineralogy on frictional sliding behavior of simulated gouges: binary and ternary mixtures of quartz, illite, and montmorillonite. J. Geophys. Res. Solid Earth 115 (B3), 1–22. https://doi.org/10.1029/2009JB006383.
- Thiercelin, M.J., Plumb, R.A., 1994. Core-based prediction of lithologic stress contrasts in east Texas formations. SPE Form. Eval. 9 (4), 251–258. https://doi.org/10.2118/21847-pa.
- Tian, J., Hao, F., Zhou, X., et al., 2014. Charging of the Penglai 9-1 oil field, Bohai Bay basin, China: functions of the delta on accumulating petroleum. Mar. Petrol. Geol. 57, 603–618. https://doi.org/10.1016/j.marpetgeo.2014.07.007.
- Tingay, M.R.P., Hillis, R.R., Swarbrick, R.E., et al., 2009. Origin of overpressure and pore-pressure prediction in the Baram province, Brunei. AAPG Bull. 93 (1), 51–74. https://doi.org/10.1306/08080808016.
- Tingay, M.R.P., Morley, C.K., Laird, A., et al., 2013. Evidence for overpressure generation by kerogen-to-gas maturation in the northern Malay Basin. AAPG Bull. 97 (4), 639–672. https://doi.org/10.1306/09041212032.
- Verberne, B.A., He, C., Spiers, C.J., 2010. Frictional properties of sedimentary rocks and natural fault gouge from the Longmen Shan fault zone, Sichuan, China. Bull. Seismol. Soc. Am. 100 (5B), 2767–2790. https://doi.org/10.1785/0120090287.
- Wang, K.J., 2016. Structural Characteristics of the Shahejie Formation and its Effects on Reservoir-Forming in BZ 34-2/4 Oilfield, Bozhong Depression. China University of Petroleum, Beijing.
- Wang, H.X., Fu, X.F., Fan, M.X., et al., 2022. Fault growth and linkage: implications for trap integrity in the Qi'nan area of the Huanghua Depression in Bohai Bay Basin, China. Mar. Petrol. Geol. 145, 105875. https://doi.org/10.1016/j.marpetgeo.2022.105875.

- Warpinski, N.R., 1989. Elastic and viscoelastic calculations of stresses in sedimentary basins. SPE Form. Eval. 4 (4), 522–530.
- Wileveau, Y., Cornet, F.H., Desroches, J., et al., 2007. Complete in situ stress determination in an argillite sedimentary formation. Phys. Chem. Earth 32 (8–14), 866–878. https://doi.org/10.1016/j.pce.2006.03.018.
- Williams-Stroud, S., Bauer, R., Leetaru, H., et al., 2020. Analysis of microseismicity and reactivated fault size to assess the potential for felt events by co2 injection in the Illinois basin. Bull. Seismol. Soc. Am. 110 (5), 2188–2204. https://doi.org/10.1785/0120200112.
- Willson, S.M., Last, N.C., Zoback, M.D., et al., 1999. Drilling in South America: a wellbore stability approach for complex geologic conditions. In: SPE Latin American and Caribbean Petroleum Engineering Conference Proceedings. https://doi.org/10.2523/53940-ms.
- Wilson, M.P., Foulger, G.R., Gluyas, J.G., et al., 2017. HiQuake: the human-induced earthquake database. Seismol Res. Lett. 88 (6), 1560–1565. https://doi.org/10.1785/0220170112.
- Wiprut, D., Zoback, M.D., 2002. Fault Reactivation, Leakage Potential, and Hydro-carbon Column Heights in the Northern North Sea, vol. 11. Norwegian Petroleum Society Special Publications, pp. 203—219. https://doi.org/10.1016/S0928-8937(02)80016-9.
- Xi, Y., Li, J., Liu, G., et al., 2019. A new numerical method for evaluating the variation of casing inner diameter after strike-slip fault sliding during multistage fracturing in shale gas wells. Energy Sci. Eng. 7 (5), 2046–2058. https://doi.org/ 10.1002/ese3.410.
- Xu, K., Liu, Y., Yang, J., et al., 2011. Prediction technique of wellbore stability for scientific exploration well in Bohai Oilfield. Fault-Block Oil Gas Field 18 (5), 660–662.
- Yielding, G., Freeman, B., Needham, D.T., 1997. Quantitative fault seal prediction. AAPG Bull. 81 (6), 897–917. https://doi.org/10.1306/522b498d-1727-11d7-8645000102c1865d.
- Zhang, X.L., Fu, X.F., Wang, Y.C., et al., 2022. Dynamic sealing behavior of sand self-juxtaposition windows on a trap-bounding fault in a natural gas storage site. Lithosphere 2022 (Special 12), 1–12. https://doi.org/10.2113/2022/9111839.
- Zhang, L., He, C., 2013. Frictional properties of natural gouges from Longmenshan fault zone ruptured during the Wenchuan Mw7.9 earthquake. Tectonophysics 594, 149–164. https://doi.org/10.1016/j.tecto.2013.03.030.
- Zhou, H., Wang, W., Wang, S., et al., 2005. Development practice of BZ34-2/4 Oilfield and some cognitions. China Offshore Oil Gas 17 (5), 36–38.
- Zoback, M.D., 2007. Reservoir Geomechanics. Cambridge university press. https://doi.org/10.1017/CBO9780511586477.
- Zoback, M.D., Harjes, H.P., 1997. Injection-induced earthquakes and crustal stress at 9 km depth at the KTB deep drilling site, Germany. J. Geophys. Res. Solid Earth 102 (B8), 18477—18491. https://doi.org/10.1029/96jb02814.
- Zoback, M.D., Moos, D., Mastin, L., et al., 1985. Well bore breakouts and in situ stress. J. Geophys. Res. 90 (B7), 5523–5530. https://doi.org/10.1029/JB090iB07p05523.